PAPER

Check for updates

Ruthenium oxychloride supported by manganese oxide for stable oxygen evolution in acidic media†

Yunxing Zhao,‡[a] Jun Hu, [ID] ‡[b] Chao-Lung Chiang, [ID] [c] Ying Li,[a] Weichuang Yang,[d] Zhenhai Yang,[d] Wei-Hsuan Hung,[e] Yan-Gu Lin,[c] Zhong Chen, [ID] [f] Bin Li,[a] Pingqi Gao [ID] *[a] and Hong Li [ID] *[ghi]

Despite the recent advances in enhancing the durability and reducing the overpotential of ruthenium (Ru)-based electrocatalysts for acidic oxygen evolution reaction (OER), their stability hardly meets the requirement of practical application. Moreover, a cost-effective strategy to stabilize the highly active but unstable Ru species is desirable. Herein, we report a stable electrocatalyst for acidic OER by dispersing the Ru oxychloride active species into a manganese oxide support (RuOCl@MnO$_x$) to form highly dispersed Ru−O−Mn without the alteration of vibrational modes and bond parameters of the MnO$_6$ group, as suggested by Raman and synchrotron radiation characterization studies. The catalyst is stable for continuous operation over 280 h with an overpotential of 228 mV at 10 mA cm^{-2} and over 200 h at 100 mA cm^{-2}, among the most stable low-mass-loading Ru-based OER electrocatalysts in acidic media. Complementary theoretical calculations ascribe the excellent stability to its high oxidation potential and low formation/surface energies, consistent with experimental observations. The enhanced activity is attributed to the four-coordinated Ru site that bears a low overpotential determined by the formation of O* from OH*. Our work thus offers a new strategy for synthesizing robust OER electrocatalysts of PEM electrolyzers with superior activity.

Introduction

Hydrogen fuel is regarded as a promising energy carrier to replace conventional fossil fuels for a sustainable energy future.[1] A clean and sustainable hydrogen economy can be truly established only when hydrogen is made from water splitting

[a]*School of Materials, Sun Yat-sen University, Guangzhou 510275, China. E-mail: gaopq3@mail.sysu.edu.cn*

[b]*School of Chemical Engineering, Northwest University, Xi'an 710069, China*

[c]*Scientific Research Division, National Synchrotron Radiation Research Center, Hsinchu 30076, Taiwan*

[d]*Ningbo Institute of Material Technology and Engineering, Chinese Academy of Sciences, Ningbo 315201, China*

[e]*Institute of Materials Science and Engineering, National Central University, Taoyuan 320317, Taiwan*

[f]*School of Materials Science and Engineering, Nanyang Technological University, 639798, Singapore*

[g]*School of Mechanical and Aerospace Engineering, Nanyang Technological University, 639798, Singapore*

[h]*CINTRA, CNRS/NTU/THALES, UMI 3288, Research Techno Plaza, 637553, Singapore*

[i]*Centre for Micro-/Nano-electronics (NOVITAS), School of Electrical and Electronic Engineering, Nanyang Technological University, 639798, Singapore. E-mail: ehongli@ntu.edu.sg*

† Electronic supplementary information (ESI) available: Experimental details, additional materials characterization data, electrochemical results, and computation details. See https://doi.org/10.1039/d2ta05335g

‡ Equally contributed to this work.

technology driven by renewable energy sources such as wind and solar.[2] Proton-exchange membrane (PEM) electrolysis for hydrogen production has demonstrated many exclusive advantages over alkaline water electrolysis, including higher current density, higher purity of pressurized hydrogen, a more compact and portable electrolyzer system, and importantly, much better compatibility with intermittent/discontinuous renewable energy sources.[1,3] Nevertheless, large-scale implementation of a PEM electrolyzer has been restricted by its precious catalysts, particularly the lack of a durable, efficient, and cost-effective electrocatalyst for the oxygen evolution reaction (OER) in harsh acidic media. The state-of-the-art OER catalysts are scarce and precious iridium oxide (IrO$_2$) and ruthenium oxide (RuO$_2$), both of which are perched on top of the OER volcano plot due to their high intrinsic activities.[4] RuO$_2$ has a lower cost and higher OER activity but poorer stability than IrO$_2$.[5] Hence, developing affordable Ru-based catalysts with long-term operation stability is of great significance for the widespread deployment of PEM electrolysis technology.

An inherent low oxidation potential of 1.39 V *versus* RHE (reversible hydrogen electrode) to form soluble ruthenium tetroxide (RuO$_4$) renders RuO$_2$ less stable under OER operating conditions (>1.23 V *vs.* RHE), leading to a narrow stable operating potential window.[6] Besides, the participation of lattice oxygen of RuO$_2$ to evolve O$_2$ during the OER process also accelerates its degeneration due to corrosion.[7] Moreover, the

20964 | *J. Mater. Chem. A*, 2022, **10**, 20964–20974

This journal is © The Royal Society of Chemistry 2022

calculated free energy change of the rate determining step (RDS) in the four-step OER reaction is very high at the RuO_2 surface, signifying a sluggish kinetic process.[8] To this end, tremendous efforts have been dedicated to improving both stability and activity of Ru-based OER catalysts. For instance, vacancy engineering,[9] structural defect formation,[10,11] element doping,[12] metal alloying,[13] solid solution design,[8] the single atom strategy,[14] structure engineering of $SrRuO_3$ perovskite/$A_2Ru_2O_7$ pyrochlore,[15,16] crystal plane/phase engineering,[17] and novel catalysts such as RuB_2,[18] have been reported to exhibit good OER performance, with much lower overpotentials and significantly improved stability (up to 24 h) than those of pristine RuO_2 (<4 h)[12,19] in delivering a benchmark current density of 10 mA cm^{-2}. However, many approaches focus on structural modification of the crystal or crystalline phase, as well as doping or compounding based on the ruthenium oxide itself, which inevitably introduce the RuO_2 crystal in the catalyst, leading to oxidative degradation (by forming soluble RuO_4) at low anodic potentials under acidic conditions. A method capable of deconstructing the RuO_2 crystal and inhibiting the Ru–O–Ru bonds is expected to greatly enhance the stability of Ru-based OER catalysts.

Moreover, the supporting material for catalysts has been proven to play a key role in catalysis, which reduces the possibility of agglomeration and increases the specific surface area, resulting in better dispersion of active catalyst species and more efficient atom utilization.[20,21] Besides, the metal–support interaction is often observed for improving interfacial electron transfer,[22] tailoring the binding strength,[20] or inducing surface species migration (e.g., hydrogen spillover).[23] Towards acidic OER, a supporting material can enhance the stability of catalysts in extremely harsh, corrosive, and oxidative environments. Cerium dioxide (CeO_2), titanium dioxide (TiO_2), chromium dioxide (CrO_2), manganese dioxide (MnO_2), titanium (Ti), tellurium (Te), and carbon (C) as potential candidates of supporting materials have demonstrated superb acid and oxidation resistance as evidenced by their nanocomposite (e.g., Co_3O_4/CeO_2),[24] composite catalyst (e.g., IrO_2–TiO_2),[25] solid solution (e.g., $Cr_{0.6}Ru_{0.4}O_2$),[8] and catalyst on supports (e.g., IrO_2/MnO_2, H-Ti@IrO_x, IrRu@Te, and RuIr@CoNC).[26–29] Notably, individual gamma (γ)-phase MnO_2 as a nonprecious OER catalyst shows stable operation over 8, 000 h at 10 mA cm^{-2} in an acidic electrolyte (pH of 2), indicating its inherent chemical stability; although the overpotential (428 mV) is much inferior to that of RuO_2 (310 mV).[30]

Herein, a stable Ru-based OER catalyst is rationally constructed by dispersing the Ru oxychloride active species into a solid MnO_x supporting material, where Ru is the actual active site, and the doped/chemisorbed Cl facilitates the dispersion of Ru and thus provides abundant active structural defects.[31,32] The rational design of the catalyst comprises: (1) the MnO_x support with high acid and oxidation resistance helps stabilize the encapsulated Ru species by inhibiting RuO_2 formation, (2) the Ru active sites significantly decrease the OER overpotential, which in turn slows down the oxidation of the MnO_x support to MnO_4^- at high potentials, (3) the homogeneous dispersion of the active Ru sites in the MnO_x matrix results in a sustained

OER operation with high activity at low mass loading, and (4) both OER-active RuO_2 and MnO_x with strong catalyst–support interactions work synergistically to enhance the overall catalytic performance. The resulting catalyst with a low Ru mass loading of 0.105 mg$_{Ru}$ cm^{-2} (versus 1–3 mg$_{Ir}$ cm^{-2} for commercial OER catalysts used in PEM electrolyzers)[1] shows a low overpotential of 228 mV at 10 mA cm^{-2} and great stability for 280 h at 10 mA cm^{-2} and 200 h at 100 mA cm^{-2} in the strongly acidic media (0.5 M sulfuric acid, pH 0.26), outperforming most reported Ru-based OER electrocatalysts.

Results and discussion

The facile fabrication process of the anode material is illustrated in Fig. S1a.† First, a carbon fiber paper (CFP) substrate was heated to 210 °C, followed by the dropwise addition of a precursor solution containing $RuCl_3$ and $Mn(NO_3)_2$ onto the hot CFP surface (see the Experimental section, ESI†). Then, RuOCl@MnO_x was obtained after heating the CFP-loaded precursor at 210 °C for 10 min. The MnO_x or RuOCl control samples were obtained by dropwise adding individual $RuCl_3$ or $Mn(NO_3)_2$ solutions onto the CFP substrate, while RuOCl/MnO_x was obtained by dropwise adding $RuCl_3$ solution onto the as-synthesized CFP-loaded MnO_x, all of which were made by the same thermal treatment process. The CFP substrate is suitable for fabrication of a membrane electrode assembly in PEM electrolyzers owing to its excellent resistance to acid and oxidation.[30,33] Notably, this fabrication method is scalable thanks to the mild synthesis conditions and low cost of MnO_2 (10^{-4} times lower than that of RuO_2). The schematic catalyst structure of RuOCl@MnO_x is illustrated in Fig. 1a, where the Ru oxychloride (RuOCl) species is dispersed into the MnO_x support. The Ru atoms bond to O atoms to form the dominant Ru–O–Mn, and the residue Cl element is doped or chemisorbed in the catalyst after oxidation of the $RuCl_3$ precursor. A defect structure is introduced onto the MnO_x support arising from exotic Ru atoms, and the doped/chemisorbed Cl atom further increases the unsaturated coordination defects. The active Ru atoms are encapsulated by abundant Mn and O atoms, thus providing protection to the catalytic site. Such a geometry has several advantages: (1) the similar octahedral coordination of RuO_2 and MnO_2 as their crystalline phases[34] endows RuOCl@MnO_x with compatible unit structures and thus suppresses the tendency of phase segregation, (2) the amorphous characteristics arising from the low synthesis temperature increase the density of defect sites, such as grain boundaries and edges, and thus increase the catalytic activity, and (3) the MnO_x material with excellent resistance to acid corrosion and oxidation offers a reliable and stable support for the Ru catalyst, thus breaking the aggregation of ruthenium oxide and improving the oxidation potential.

The structure analysis by X-ray diffraction (XRD; Fig. 1b and S1b†) indicates the amorphous state of RuOCl@MnO_x and RuOCl, as suggested by the lack of well-defined peaks. The XRD peaks of MnO_x located at $2\theta = 33.1$, 55.2, and 66.0° correspond to the (222), (440), and (622) planes of the Mn_2O_3 structure, respectively.[35] The absence of a crystalline peak in

This journal is © The Royal Society of Chemistry 2022

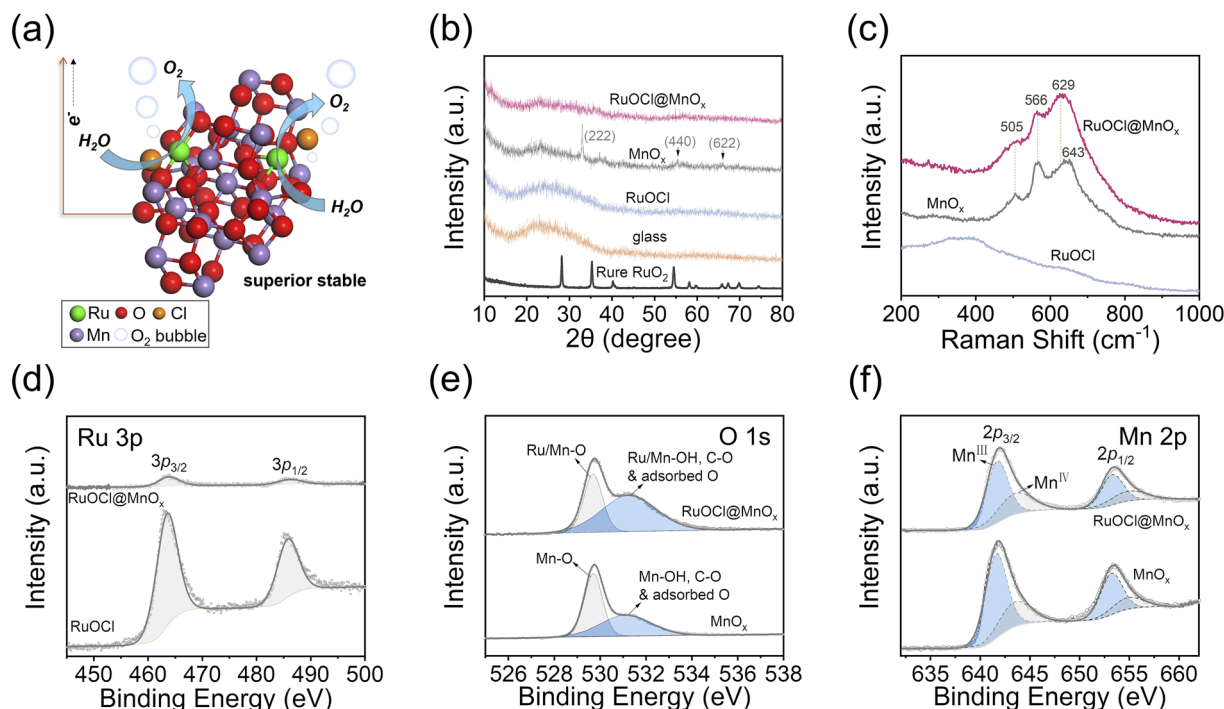J. Mater. Chem. A, 2022, **10**, 20964–20974 | **20965**

Fig. 1 (a) Schematic diagram of the oxygen evolution reaction (OER) on the catalyst by dispersing the RuOCl species onto a MnO_x support, where the green, orange, red, and purple balls represent Ru, Cl, O, and Mn atoms, respectively, and the blue circles delineate the oxygen bubbles. (b) XRD patterns of $RuOCl@MnO_x$, MnO_x, RuOCl, and pure RuO_2 samples. (c) Raman spectra of $RuOCl@MnO_x$, MnO_x, and RuOCl samples. XPS spectra of (d) Ru 3p, (e) O 1s, and (f) Mn 2p states, respectively.

$RuOCl@MnO_x$ suggests that the added Ru and Cl disturb the crystallinity of the MnO_x support. It is worth noting that crystal defects and unsaturated coordination in the RuO_2 catalyst are responsible for the highly active OER.[10,12,36] The Raman spectra (Fig. 1c) show that the peak positions of $RuOCl@MnO_x$ are close to those of MnO_x, where 505 cm^{-1}, 566 cm^{-1} (Mn–O stretching vibration in the basal plane), and 643 cm^{-1} (symmetric stretching mode of the MnO_6 group) correspond to the lattice vibration modes of MnO_2.[37,38] The RuOCl sample does not show the lattice vibration peaks observed in crystalline RuO_2.[36] It is therefore unlikely to form crystalline RuO_2 from the aqueous $RuCl_3$ precursor by treatment at 210 °C for 10 min, whereas crystalline MnO_x can be obtained by pyrolysis of $Mn(NO_3)_2$ under these conditions. The elemental composition analyses were conducted by X-ray photoelectron spectroscopy (XPS) for Ru 3p, Cl 2p, Mn 2p, and O 1s states. The full XPS spectrum in Fig. S2a† covers Ru, O and Cl elements in catalysts $RuOCl@MnO_x$ and RuOCl, as well as Mn and O elements from the MnO_x support. Ru 3p peaks located at 463.8 and 486.2 eV (Fig. 1d) and Ru 3d peaks at 281.3 and 285.5 eV (Fig. S2b†) are assigned to the Ru^{4+} state.[10,39] We note that the intensity of Ru in $RuOCl@MnO_x$ is much weaker than that in RuOCl even at the same Ru loading, indicating good dispersion of Ru into the MnO_x matrix. Notably, a significant Cl signal is observed in both $RuOCl@MnO_x$ and RuOCl (Fig. S2c†) at 198.1 eV and 199.8 eV, corresponding to Cl $2p_{3/2}$ and Cl $2p_{1/2}$ of Cl$^-$.[40] The Cl could not be completely removed despite the thorough cleaning of the prepared sample, suggesting that the Cl element has been doped or chemically adsorbed in the catalyst. In addition, the O

1s spectra (Fig. 1e) can be deconvoluted as the lattice oxygen (529.7 eV) and hydroxyl groups/C–O/adsorbed oxygen on the surface (531.2 eV).[10,11] The Mn $2p_{3/2}$ signals located at 641.7 eV and 643.6 eV (Fig. 1f) in $RuOCl@MnO_x$ and MnO_x are assigned to Mn^{3+} and Mn^{4+} states,[41] respectively, with a ratio of ~1.8 ($Mn^{3+} : Mn^{4+}$) in $RuOCl@MnO_x$. Moreover, the Ru : Cl : O : Mn ratio (1 : 0.8 : 15.5 : 7.8) in $RuOCl@MnO_x$ was obtained by semi-quantitative analysis of XPS (Fig. S2d†), which reveals that each Ru catalytic site is surrounded by 8 Mn atoms, suggesting its good dispersion. In contrast, the Cl content is significantly less in RuOCl (Ru : Cl : O = 1 : 0.2 : 2.1), suggesting that some Cl would be doped or chemisorbed into the MnO_x. And the Mn : O (1 : 1.8) ratio in MnO_x implies a mixture of polycrystalline Mn_2O_3 and amorphous MnO_2 in the MnO_x support, consistent with XRD analysis. The K-edge XANES spectra are analyzed to further confirm the oxidation states of Ru and Mn, by fitting the Ru/Mn oxidation states as a function of the Ru/Mn K-edge energy shifts (Fig. S3†), and the average valence states of Ru and Mn are $Ru^{3.9+}$ and $Mn^{2.8+}$, respectively.

The high-resolution transmission electron microscopy (HRTEM) image in Fig. 2a shows that the $RuOCl@MnO_x$ is composed of amorphous nanoparticles with tiny nanocrystals, where a d-spacing of 0.27 nm corresponds to the (222) plane of Mn_2O_3.[42] Besides, the selected area electron diffraction (SAED, Fig. 2b) patterns show faint diffraction rings corresponding to the (222), (411), (521) and (622) planes of Mn_2O_3, further illustrating the polycrystalline and amorphous composition of $RuOCl@MnO_x$.[43–45] The absence of RuO_2 nanocrystals indicates great dispersion of Ru in the MnO_x support. The image taken by

20966 | J. Mater. Chem. A, 2022, 10, 20964–20974

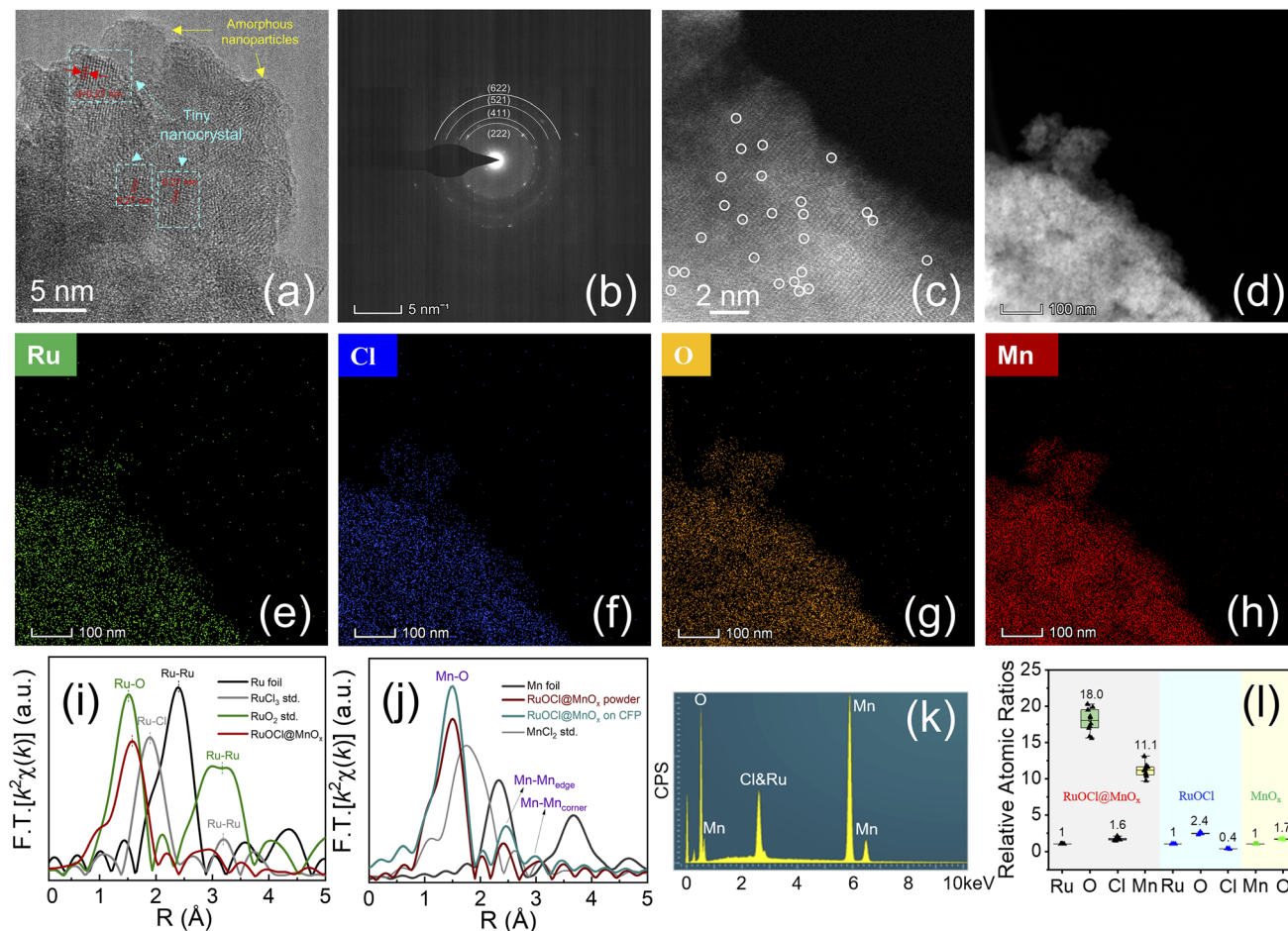This journal is © The Royal Society of Chemistry 2022

Fig. 2 (a) HRTEM image, the (b) SAED pattern, and (c) AC-HAADF-STEM image of RuOCl@MnO$_x$. (d) HAADF-STEM image and corresponding STEM-EDS mappings of (e) Ru, (f) Cl, (g) O, and (h) Mn, respectively. (i) Ru K-edge FT-EXAFS spectra of RuOCl@MnO$_x$, RuO$_2$, RuCl$_3$, and Ru foil. (j) Mn K-edge FT-EXAFS spectra of RuOCl@MnO$_x$ powder, RuOCl@MnO$_x$ on CFP, MnCl$_2$, and Mn foil. (k) Energy dispersion spectrum of RuOCl@MnO$_x$. (l) Atomic ratios obtained from the EDS results, where the atomic concentrations are normalized to that of Ru in RuOCl@MnO$_x$ and RuOCl and to that of Mn in MnO$_x$.

aberration-corrected high-angle annular dark-field scanning transmission electron microscopy (AC-HAADF-STEM, Fig. 2c) shows that some individual metal atoms (*i.e.*, Ru and Mn) are well anchored on the surface of the MnO$_x$ support as distinguishable bright spots marked with circles. The element distributions in RuOCl@MnO$_x$ were determined by scanning TEM energy dispersive X-ray spectroscopy (STEM-EDS), and the images show that all elements including Ru, Cl, O, and Mn exhibit a uniform distribution (Fig. 2d–h) in the catalyst. The Fourier transforms (FTs) of the Ru K-edge $k^2\chi(k)$ spectra (Fig. 2i) show that the Ru–O peak shifts to 1.57 Å of RuOCl@MnO$_x$ from 1.50 Å of RuO$_2$, which is attributed to the change in the local coordination environment induced by the dominant Ru–O–Mn bond in RuOCl@MnO$_x$.[46,47] The FTs of the Mn K-edge $k^2\chi(k)$ spectra (Fig. 2j), where 1.5, 2.4 and 3.0 Å match the Mn–O bond, the edge-sharing Mn–Mn$_{edge}$, and the corner-sharing Mn–Mn$_{corner}$ in the MnO$_6$ octahedra, respectively,[48] suggest that the MnO$_6$ octahedral framework in the MnO$_x$ support is maintained despite the introduction of external elements, which is consistent with the Raman measurement results. In contrast to

the Ru–Cl (1.90 Å) and Mn–Cl (1.75 Å) coordination in the first shells of Ru and Mn central atoms in RuCl$_3$ and MnCl$_2$, respectively, the peaks at 1.57 Å and 1.5 Å in RuOCl@MnO$_x$ (Fig. 2i and j) correspond to the Ru–O and Mn–O coordination in the first shells of Ru and Mn sites, respectively. This suggests that the Ru–Cl coordination in RuCl$_3$ is replaced by Ru–O during the thermal treatment, while the Mn–O coordination is generated during the pyrolysis of Mn(NO$_3$)$_2$. A large number of Cl atoms in the non-first coordination shell of Ru or Mn centers may physically or chemically interact with O atoms, resulting in the adsorption or doping state, which is not detected in the K-edge FT-EXAFS spectra.[49,50] In addition, the electron energy loss spectroscopy (EELS) pattern (Fig. S4†) shows that only Mn and O signals appear in RuOCl@MnO$_x$, in contrast to the obvious Ru and Cl peaks in RuOCl. The absence of Ru and Cl peaks due to the encapsulation by the manganese oxide support suggests that RuOCl has been uniformly dispersed in the MnO$_x$ matrix rather than segregated on the surface. The SEM images (Fig. S5†) show that both RuOCl@MnO$_x$ and MnO$_x$ are densely deposited on the CFP surface; however, the coverage of RuOCl is

poor. SEM-EDS analysis was also employed to quantify the elemental content (Fig. S6†), which shows the uniform distribution of Ru, Cl, O, and Mn on the deposited membrane. The Ru : Cl : O : Mn (1 : 1.6 : 18.0 : 11.1) ratios in RuOCl@MnO$_x$ (see Fig. 2k for the spectrum) and the Ru : Cl : O (1 : 0.4 : 2.4) ratios in RuOCl (Fig. 2l) obtained from EDS indicate that the proportion of Cl is higher by EDS than that by XPS, suggesting that more Cl is doped or chemisorbed beneath the surface. Furthermore, the Mn : O (1 : 1.7) ratio measured by EDS is close to that obtained by XPS, suggesting a mixture of polycrystalline Mn$_2$O$_3$ and amorphous MnO$_2$. The loading mass of Ru in RuOCl@MnO$_x$ is 0.112 mg cm^{-2} (calculated as MW = 207.43 g mol^{-1} for RuCl$_3$·H$_2$O) or 0.105 mg cm^{-2} [based on inductively coupled plasma optical emission spectrometry (ICP-OES)], corresponding to 0.15 mg or 0.14 mg pristine RuO$_2$, respectively. ICP-OES (Fig. S7†) also gives the Ru : Mn (1 : 9.6) ratio in RuOCl@MnO$_x$, which is close to those estimated from EDS or XPS analysis (Table S1†).

Electrochemical tests were carried out on a three-electrode setup with a catalyst-coated CFP as the working electrode (Fig. S8†) to evaluate the stability and activity of the catalyst. The stability test was recorded as shown in Fig. 3a, which exhibits the potential change at a constant OER current density of 10 mA cm^{-2}. The RuOCl@MnO$_x$ catalyst displays stable operation up to 280 h with only a 50 mV overpotential increase, corresponding to a degradation rate of 0.18 mV h^{-1}. Notably, most of the degradation (46%) occurs in the first 25 h (the inset of Fig. 3a). This superior stability outperforms most Ru-based OER electrocatalyst operating in acidic media (see Table S2† for comparison), while being comparable to other support-loaded Ru/Ir catalysts.[27–29] In contrast, both pristine RuO$_2$ (denoted as RuO$_2$|x@CFP, with x representing the RuO$_2$ mass loading by dispersing RuO$_2$/Nafion/water/ethanol ink on CFP, see the Experimental section in the ESI†) and RuOCl exhibit rapid activity decay. Specifically, RuO$_2$|0.15@CFP and RuO$_2$|1.05@CFP (with 1 and 7 times as much Ru mass loading as that in RuOCl@MnO$_x$, respectively) completely deactivate within 0.05 h and 10 h, respectively, consistent with previous reports of rapid RuO$_2$ degradation.[8,19] Meanwhile, the potential of RuOCl increases from 1.44 to 2 V within 4 h, corresponding to a degradation rate of 140 mV h^{-1}. Moreover, the relatively steady OER potential of MnO$_x$ with a minor increase from 1.86 V to 1.93 V over 20 h discloses its high antioxidant capability but inferior OER activity. These comparisons suggest that Ru is the active site, and MnO$_x$ acts as the supporting material, endowing RuOCl@MnO$_x$ with superior stability and activity. Additionally, we note that the potentials of RuOCl/MnO$_x$ and RuO$_2$/MnO$_x$ (prepared by dropping RuO$_2$/Nafion/water/ethanol dispersion ink onto the surface of the as-synthesized CFP-loaded MnO$_x$) undergo a much slower decrease to 1.54 V and 1.79 V in 30 h and 20 h, respectively, compared to the rapid deactivation of RuOCl (4 h) and RuO$_2$|0.15@CFP (0.05 h), signifying that MnO$_x$ also stabilizes the catalyst even by simple loading on its surface. We hypothesize that the enhanced durability of RuOCl/MnO$_x$ and RuO$_2$/MnO$_x$ is ascribed to the valence state and structural transformation of MnO$_x$ during the OER process that will be detailed later. However, the Ru content of RuO$_2$/MnO$_x$ is

reduced due to the degradation of surface RuO$_2$, similar to that of pure RuO$_2$ in the stability test. The inhomogeneous structure of Ru, which is physiochemically adsorbed at the RuO$_2$ and MnO$_x$ interface or encapsulated in structurally transformed MnO$_x$, makes RuO$_2$/MnO$_x$ less active than RuOCl@MnO$_x$. Steady OER operation at high current densities accelerates the oxidative failure of the catalyst, and thus it is an important consideration in practical applications. We therefore tested the stability at higher current densities of 100 mA cm^{-2}, 300 mA cm^{-2} and 500 mA cm^{-2} as shown in Fig. 3b. After 200 h continuous operation at 100 mA cm^{-2}, the overpotential increment is 115 mV, corresponding to a degradation rate of 0.6 mV h^{-1}. The degradation accelerates at 300 mA cm^{-2} (164 mV degradation in 100 h) and 500 mA cm^{-2} (346 mV degradation in 50 h).

Next, we evaluated the activity of the catalyst RuOCl@MnO$_x$ from the linear scanning voltammetry (LSV) curves (Fig. 3c). RuOCl@MnO$_x$ exhibits excellent activity with an onset potential (the potential at a current density of 1 mA cm^{-2}) of 1.41 V and an overpotential of only 228 mV at 10 mA cm^{-2}. In contrast, the onset potentials of RuO$_2$|0.15@CFP and RuO$_2$|1.05@CFP are much higher, reaching 1.52 V and 1.47 V, respectively. The overpotential of RuO$_2$|1.05@CFP is 306 mV at a current density of 10 mA cm^{-2} (Fig. 3d). RuO$_2$|1.05@CFP and RuO$_2$|0.15@CFP show small current densities of 32 and 5 mA cm^{-2} (*vs.* 118 mA cm^{-2} of RuOCl@MnO$_x$) at 1.6 V. Moreover, a high onset potential of 1.76 V and a high overpotential of 620 mV at 10 mA cm^{-2} for MnO$_x$ also indicate that the active site is not derived from the MnO$_x$ support. In addition, RuOCl suffered a rapid decay in the potential scan test (Fig. S9†). It is noted that RuO$_2$|0.15@CFP with the same Ru mass loading as that of RuOCl@MnO$_x$ (calculated as MW = 207.43 g mol^{-1} for RuCl$_3$·H$_2$O) has a much higher overpotential than 306 mV when driving a current density of 10 mA cm^{-2}, consistent with the previous reports.[36] Upon gradually increasing the Ru loading (Fig. S10a†), the overpotential of RuO$_2$|1.05@CFP reaches 306 mV, which is close to that of RuO$_2$ loaded on a glassy carbon electrode (~0.275 mg cm^{-2}).[12] Such inferior performance is attributed to the fact that the loaded RuO$_2$ nanoparticles (TEM image in Fig. S10b†) are partially trapped in the interfibrillar voids of CFP and therefore cannot participate efficiently in the catalytic reaction. The mass activity (Fig. S11†) of RuOCl@MnO$_x$ is as high as 481 A g$_{Ru}^{-1}$ at η = 300 mV, which is 41 times higher than that of RuO$_2$|1.05@CFP or RuO$_2$|0.15@CFP (Fig. 3d). Although the mass activity of catalysts with active sites uniformly dispersed inside the support is relatively low compared to those with active sites dispersed on the support surface,[27–29] RuOCl@MnO$_x$ is still one of the most superior low-mass-loading Ru- and Ir-based electrocatalysts (see Table S2† for details). Notably, the Tafel curve (Fig. 3e) of RuOCl@MnO$_x$ (43 mV dec^{-1}) is smaller than those of RuO$_2$|1.05@CFP (48 mV dec^{-1}) and RuO$_2$|0.15@CFP (53 mV dec^{-1}), indicating faster OER kinetics.

We examined the structural stability of the catalyst after 280 h stability testing. Compared with the initially rough and dense membranes (Fig. S12a–c†), the catalyst appears to resemble the nanosheet structure of MnO$_2$ after stability testing
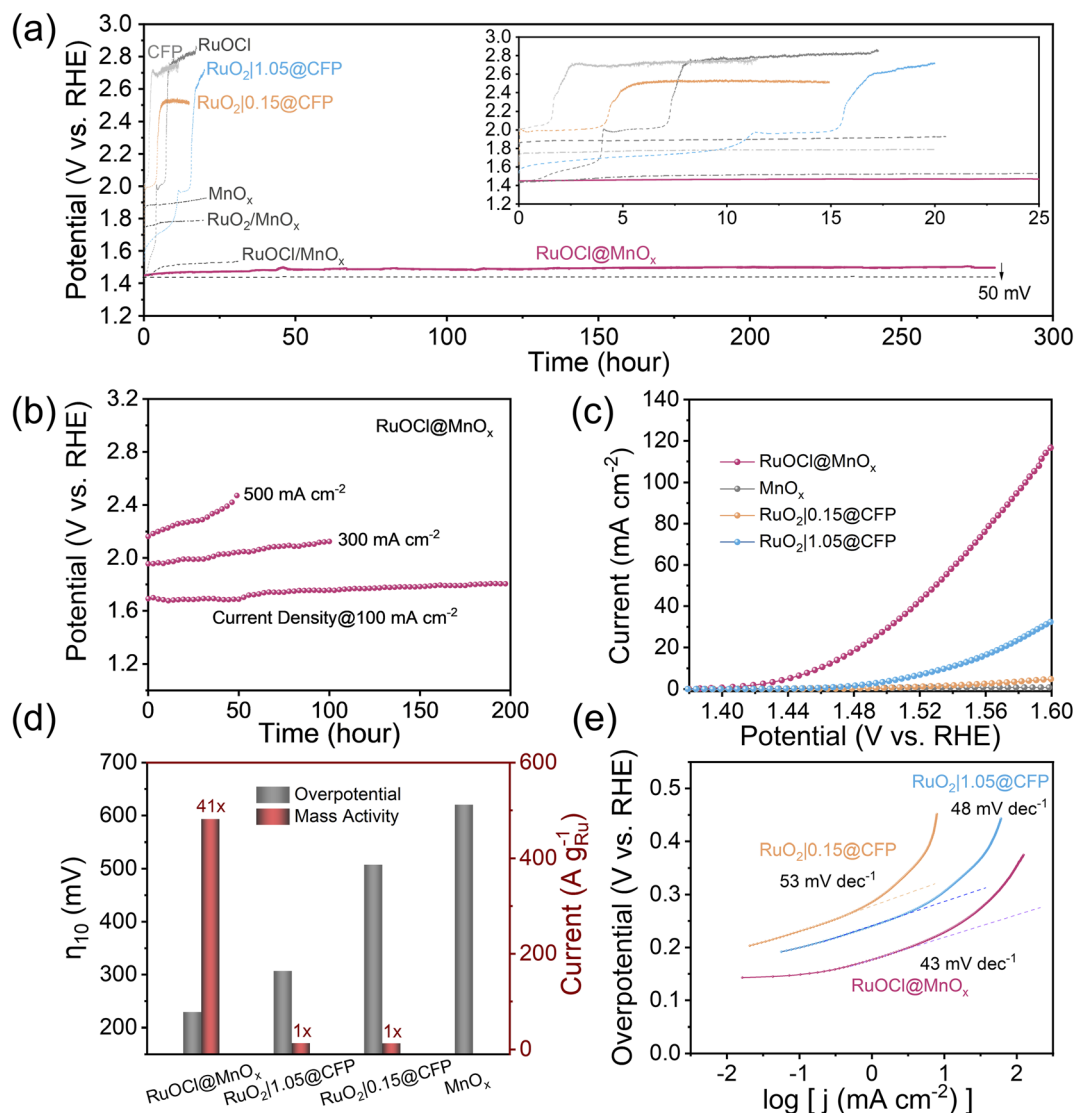
20968 | *J. Mater. Chem. A*, 2022, **10**, 20964–20974

This journal is © The Royal Society of Chemistry 2022

Fig. 3 (a) Chronopotentiometry curves of RuOCl@MnO$_x$, RuOCl, MnO$_x$, RuO$_2$|0.15@CFP, RuO$_2$|1.05@CFP, RuOCl/MnO$_x$, RuO$_2$/MnO$_x$, and CFP at a current density of 10 mA cm^{-2}. The inset is the enlarged curves within 25 h. (b) Chronopotentiometry curves of RuOCl@MnO$_x$ at current densities of 100 mA cm^{-2}, 300 mA cm^{-2}, and 500 mA cm^{-2} without *iR* correction. (c) Polarization curves of RuOCl@MnO$_x$, RuO$_2$|0.15@CFP, RuO$_2$|1.05@CFP, and MnO$_x$. (d) Overpotentials at 10 mA cm^{-2} (η_{10}) of RuOCl@MnO$_x$, RuO$_2$|1.05@CFP, RuO$_2$|0.15@CFP, and MnO$_x$, and mass activities of RuOCl@MnO$_x$, RuO$_2$|1.05@CFP, and RuO$_2$|0.15@CFP at an overpotential of 300 mV. (e) Tafel plots of RuOCl@MnO$_x$, RuO$_2$|1.05@CFP, and RuO$_2$|0.15@CFP.

(Fig. S12d–f†). The Raman peaks are slightly shifted to 497 cm^{-1}, 572 cm^{-1}, and 651 cm^{-1} as shown in Fig. 4a, which may have originated from the changes in the valence state and bond length.[51,52] The newly appeared peak located at 385 cm^{-1} corresponds to the bending mode of Mn–O–Mn.[53] However, the XRD pattern (Fig. S13†) does not show any crystalline MnO$_2$ peak, which suggests a predominantly amorphous phase of MnO$_2$. It is still possible to observe some tiny nanocrystals with a lattice spacing of 0.36 nm by HRTEM (Fig. S14†), which corresponds to the (002) plane of δ-MnO$_2$,[54] suggesting the transformation of the MnO$_x$ support during the catalysis process. The XPS and normalized Ru K-edge XANES spectra of RuOCl@MnO$_x$ after 48 h testing (Fig. 4b and c) show no significant degradation of the Ru active site during the early stages of long-term catalysis. The Mn K-edge XANES spectra

shift from an energy close to Mn$_2$O$_3$ (Mn^{3+} reference) towards that of MnO$_2$ (Mn^{4+} reference) after 48 h testing, while a significant positive shift of the Mn 2p peak is observed by XPS after 280 h (Fig. 4d and e). Concurrently, the Mn^{3+}/Mn^{4+} ratio gradually decreases from 1.8 (initially) to 1.1 (after 280 h), further indicating an increase in MnO$_2$, which is consistent with the morphological and Raman characterization studies. Doped/chemisorbed Cl (Fig. 4f) is closely related to the degradation of the catalyst. With the Cl peak disappearing after the 280 h test, apparent degradation occurs thereafter. In addition, the O 1s peak (Fig. S15†) of lattice oxygen shifts slightly after the 280 h test, which could be attributed to the composition, valence state, and microstructure of the redeposited MnO$_2$ nanosheet.[55,56] The weights of Mn and Ru ions dissolved in solution after 280 h stability testing are 0.08 mg and 0.07 mg,

This journal is © The Royal Society of Chemistry 2022

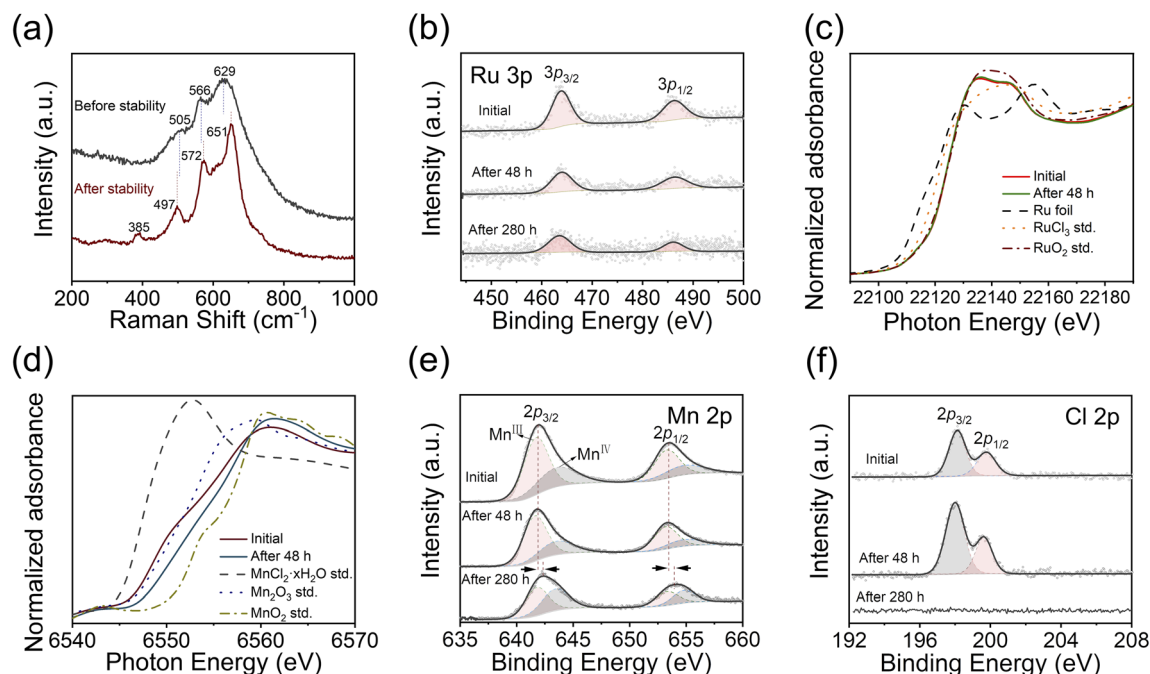*J. Mater. Chem. A*, 2022, **10**, 20964–20974 | **20969**

Fig. 4 (a) Raman spectra of RuOCl@MnO$_x$ before and after the 280 h stability test. (b) XPS spectra of the Ru 3p state of initial RuOCl@MnO$_x$, and that after the 48 h stability test and after the 280 h stability test. (c) Normalized Ru K-edge XANES spectra of initial RuOCl@MnO$_x$ and RuOCl@MnO$_x$ after the 48 h stability test, Ru foil, RuCl$_3$, and RuO$_2$. (d) Normalized Mn K-edge XANES spectra of initial RuOCl@MnO$_x$ and RuOCl@MnO$_x$ after the 48 h stability test, MnCl$_2$·xH$_2$O, Mn$_2$O$_3$, and MnO$_2$. XPS spectra of (e) Mn 2p and (f) Cl 2p states of initial RuOCl@MnO$_x$, that after the 48 h stability test, and after the 280 h stability test.

respectively, according to ICP measurement (Fig. S7†). Other dissolved Mn^{3+}, however, is redeposited on the surface in the form of MnO$_2$ nanosheets (Fig. S12 and S14†), which is consistent with a previous report.[30] Notably, the high activity of the catalyst is not significantly affected during the redeposition process of MnO$_2$ nanosheets, suggesting that the vertical structure of the nanosheets provides sufficient space for the transport of the proton and hydrogen molecule. The faradaic efficiency (electric charges involved) of the Mn/Ru ionic reactions is negligible compared to those of the OER or HER (ESI Note 1†). Moreover, sheet-like structures with morphological variations depending on the applied potentials are also observed after stability tests at high current densities (Fig. S16†), and the flakes are dominated by the amorphous phase as shown by HRTEM (Fig. S17†). The Raman peaks (Fig. S18†) exhibit slight shifts, accompanied by the appearance of peaks located at 385 cm^{-1} (bending vibration of Mn–O–Mn) and 720 cm^{-1} (stretching vibration of Mn–O–Mn).[53,57] Additionally, the Ru 3p peaks are significantly weakened, reflecting the imminent depletion of the active species on the catalyst surface and thus the impending rapid decay of activity, approaching the end of the stability test; furthermore, both the Mn 2p and O 1s peaks show similar positive shifts (Fig. S19†). The Mn and Ru ions undergo more rapid dissolution at high anodic potentials as revealed by ICP-OES characterization (Fig. S7b†).

MnO$_2$ and RuO$_2$ corrode via the following reactions, MnO$_2$ + 2H$_2$O → MnO$_4^-$ + 4H$^+$ + 3e$^-$ (E^0 = 1.70 V vs. RHE)[58] and RuO$_2$ +

2H$_2$O → RuO$_4$(aq) + 4H$^+$ + 4e$^-$ (E^0 = 1.39 V vs. RHE).[6] For the durability test, the MnO$_x$ catalyst support remains stable for at least 20 h in the range of 1.86 to 1.93 V (Fig. 3a). Our calculated Pourbaix diagram (Fig. S20†) of the 89–11% Mn–Ru system in aqueous solution also demonstrates a higher oxidation potential of MnO$_2$ than RuO$_2$. We also performed a slow scan (0.1 mV s^{-1}) LSV experiment extended to high anodic potentials (Fig. 5a), and the results show that the OER dominates prior to catalyst degradation, and the significant degradation occurs at the clear inflection points of OER current. For RuO$_2$|0.15@CFP, RuOCl@MnO$_x$, and MnO$_x$, the potentials at the inflection points are 1.76 V, 2.49 V, and 2.55 V, respectively. One can see that the MnO$_x$ support greatly improves the oxidation potential of the RuOCl@MnO$_x$ catalyst. It is noteworthy that the elevated oxidation potential is crucial for enhancing the stability. The dissolution of the RuO$_2$ lattice, which is triggered by the loss of lattice/surface oxygen accompanied by the sharing of OER intermediates,[7,59] depends on the applied potential, and it becomes more severe when the potential is much higher than the theoretical redox potential (1.39 V$_{RHE}$, pH 0)[6]. The dispersion of Ru into the MnO$_x$ support results in a high oxidation potential of the catalyst and therefore long-term stability even at high current density.

In view of the predominantly amorphous characteristic of the catalyst, the catalytic reaction may involve the participation of lattice/surface oxygen.[60] Distinct from the Ru–O–Ru bonding in conventional RuO$_2$, the Ru–O–Mn bonding dominates here as a Ru atom can be surrounded by nearly ten times as many Mn

20970 | J. Mater. Chem. A, 2022, 10, 20964–20974

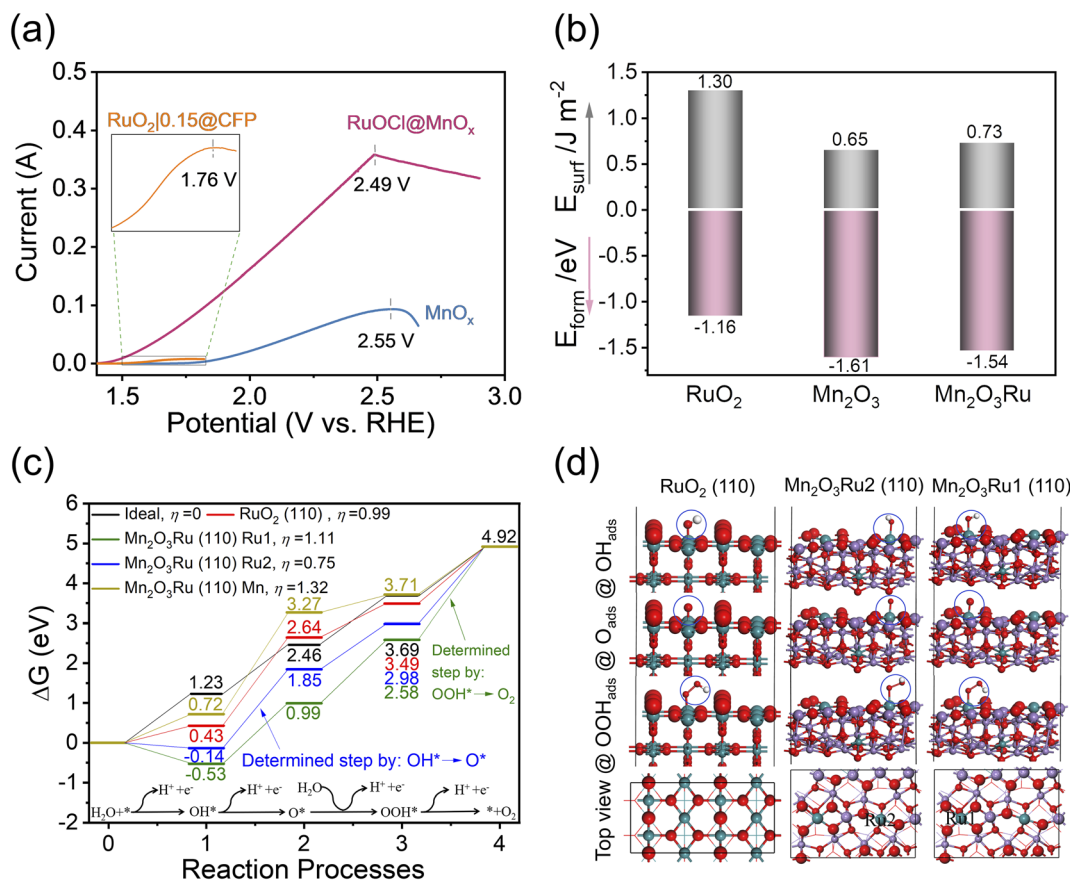This journal is © The Royal Society of Chemistry 2022

Fig. 5 (a) Slow scan linear scanning voltammetry (LSV) curves extended to a high anodic potential without *iR* correction. (b) Formation energies of bulk and (010) surface energies for RuO_2, Mn_2O_3, and Mn_2O_3Ru. (c) Free-energy profiles of the OER on different surfaces; the black line is the ideal catalyst. The unit of Gibbs free energy is eV. (d) The geometric structure and intermediates for the OER on different surfaces, where Ru (green), Mn (purple), O (red), and H (white) atoms are shown in colored spheres.

atoms according to ICP-OES tests (Table S1†). Due to the difference in bond length, electronegativity, and bond strength between Mn–O and Ru–O,[34,61] the $RuOCl@MnO_x$ catalyst differs from RuO_2 in terms of recovery of the catalyst structure such as oxygen vacancies. The oxygen vacancies involving lattice/surface oxygen accelerate the dissolution of RuO_2,[7] whereas the enhanced stability of the Ru catalyst is attributed to the presence of MnO_x that could promote the structure recovery and thus reduce the catalyst degradation. Therefore, we calculated the bulk formation energy and surface energy for the three models of RuO_2, Mn_2O_3, and Mn_2O_3Ru (see Fig. S21† for the simulation models and optimal bond parameters), since formation energy and surface energy are key parameters to assess the structural stability. It is worth noting that Mn_2O_3 is appropriate as the simulation model for the MnO_x support based on the experimental XRD, HRTEM, XPS and Mn K-edge XANES analyses, which show that Mn^{3+} is dominant. Moreover, the doped/chemisorbed Cl is not included in the model because it is not the first shell coordination atom for Ru or Mn central sites as suggested by the K-edge FT-EXAFS spectra (Fig. 2i and j), and it is not supposed to be directly engaged in the OER catalytic process. As depicted in Fig. 5b, the formation energies of RuO_2, Mn_2O_3 and Mn_2O_3Ru are −1.16 eV, −1.61 eV

and −1.54 eV, while the surface energies are 1.30 eV, 0.65 eV and 0.73 eV, respectively. Notably, both the bulk formation energy and surface energy of Mn_2O_3 are lower than those of RuO_2, suggesting that Mn_2O_3 is more stable than RuO_2. Moreover, it suggests that even when 9% Mn is substituted by Ru (*i.e.*, Mn_2O_3Ru), the energy is still lower than that of RuO_2, which signifies the greatly enhanced structural stability of Mn_2O_3Ru than pure RuO_2.

The calculated Gibbs free energy (Fig. 5c) for the OER process on different surfaces are displayed to evaluate the intrinsic activity. Here, we constructed simulation models of Mn_2O_3Ru with 9% Ru close to the experimentally measured value, as well as RuO_2 as a reference, as depicted in Fig. 5d. Ru serving as a surface catalysis center has an unsaturated coordination structure (the coordination number of Ru is determined by using the Calculate Bonds tool, Experimental section), where Ru in RuO_2 and Ru1 in Mn_2O_3Ru have a five-coordinated structure, and Ru2 in Mn_2O_3Ru has a four-coordinated structure, and these unsaturated sites are analogous to the lattice/surface oxygen vacancies for catalysis (Fig. S22†). The adsorbate evolution mechanism (AEM) is mainly considered here because a recent report suggests that the lattice oxygen evolution makes a negligible contribution to the overall OER activity

This journal is © The Royal Society of Chemistry 2022

J. Mater. Chem. A, 2022, **10**, 20964–20974 | **20971**

of RuO_x in acidic electrolyte.[59] The energy of O_2 in an ideal catalysis process is estimated to be $\Delta G_{O_2} = 4 \times 1.23 = 4.92$ eV since it is a four-electron-transfer process.[62] Comparing the Gibbs free energy on different surfaces, the reaction process of the Ru2 site on the Mn_2O_3Ru (110) surface is closer to the ideal catalysis process than that of pure RuO_2 and the Ru1 site on the Mn_2O_3Ru (110) surface, since the theoretical overpotentials for the Ru2 site on Mn_2O_3Ru (110), RuO_2, Ru1 site on Mn_2O_3Ru (110), and Mn site on Mn_2O_3Ru (110) surfaces are 0.75, 0.99, 1.11, and 1.32 V, respectively. The formation of O* from OH* serves as the rate determining step (RDS) for the four-coordinated Ru2 site that bears the smallest overpotential, although it is still higher than the experimental overpotential because the effects of solution and temperature are not taken into account in the modelling. In contrast, the reaction on the five-coordinated Ru1 site is limited by the formation of O_2 from OOH*, accompanied by a larger overpotential than that of RuO_2. The large overpotential of the Mn site also illustrates its role as a supporting material. In addition, a very large overpotential is observed if Cl is considered as the first-shell coordination atom for Ru and Mn sites (Fig. S23†), which further suggests that Cl does not bond directly to the metal atoms, in agreement with the FT-EXAFS results. Nevertheless, Cl can indirectly enhance the catalytic performance of Ru by enriching the defect sites and facilitating the dispersion of Ru. Overall, the enhanced activity is related to the four-coordinated unsaturated ruthenium structure in the $RuOCl@MnO_x$ catalyst.

Conclusions

We have developed a stabilization strategy by dispersing catalytically active RuOCl species into a low-cost MnO_x support to obtain a cost-effective, active, and stable OER electrocatalyst in an acidic electrolyte. The catalyst delivers 10 mA cm^{-2} at an overpotential of 228 mV, a mass activity of 481 A g_{Ru}^{-1} at an overpotential of 300 mV, and a Tafel slope of 43 mV dec^{-1}. More importantly, it exhibits excellent stability for 280 hours at 10 mA cm^{-2}, far exceeding those of pristine RuO_2 or support-free RuOCl catalysts. Stable operation over 200, 100, and 50 hours at 100, 300, and 500 mA cm^{-2}, respectively, has been demonstrated. Combining synchrotron radiation and other characterization studies, the outstanding stability is attributed to the synergistic effect of the catalytic species and the support, where the MnO_x support with high resistance to acid and oxidation increases the oxidation potential and slows down the oxidative corrosion of Ru, while the Ru active sites allow the OER to occur at low potentials that in turn suppresses the corrosion of the MnO_x support. Our complementary theoretical investigations disclose that the dispersion of RuOCl into the MnO_x support increases the oxidation potential and lowers the bulk formation and surface energies. As a result, the durability of the catalyst is drastically enhanced. Notably, the four-coordinated Ru site in the catalyst bears a lower overpotential and thus higher activity than that pure RuO_2 catalyst. Our work offers a new strategy for making stable and active OER catalysts with low Ru loading for PEM electrolyzers.

Author contributions

Y. Z., P. G., and H. L. designed the studies and wrote the manuscript; Y. Z. carried out the experiments; J. H. carried out DFT calculations; C. C., W. H., and Y. L., performed the XAS experiments and data analysis. Y. L., W. Y., Z. Y., Z. C., and B. L., provided helpful assistance to this article. All authors discussed the results and commented on the manuscript.

Conflicts of interest

H. Li is the inventor on a patent related to this work, filed by Nanyang Technological University, Singapore (application no. 2022-228-01-SG PRV). The authors declare no other competing interests.

Notes and references

1 M. Carmo, D. L. Fritz, J. Mergel and D. Stolten, *Int. J. Hydrogen Energy*, 2013, **38**, 4901–4934.

2 S. E. Hosseini and M. A. Wahid, *Int. J. Energy Res.*, 2020, **44**, 4110–4131.

3 Y. Zhao, M. T. Tang, S. Wu, J. Geng, Z. Han, K. Chan, P. Gao and H. Li, *J. Catal.*, 2020, **382**, 320–328.

4 I. C. Man, H. Y. Su, F. Calle-Vallejo, H. A. Hansen, J. I. Martínez, N. G. Inoglu, J. Kitchin, T. F. Jaramillo, J. K. Nørskov and J. Rossmeisl, *ChemCatChem*, 2011, **3**, 1159–1165.

5 T. Weber, T. Ortmann, D. Escalera-López, M. J. Abb, B. Mogwitz, S. Cherevko, M. Rohnke and H. Over, *ChemCatChem*, 2020, **12**, 855–866.

6 C. Roy, R. R. Rao, K. A. Stoerzinger, J. Hwang, J. Rossmeisl, I. Chorkendorff, Y. Shao-Horn and I. E. Stephens, *ACS Energy Lett.*, 2018, **3**, 2045–2051.

7 K. Klyukin, A. Zagalskaya and V. Alexandrov, *J. Phys. Chem. C*, 2019, **123**, 22151–22157.

8 Y. Lin, Z. Tian, L. Zhang, J. Ma, Z. Jiang, B. J. Deibert, R. Ge and L. Chen, *Nat. Commun.*, 2019, **10**, 162.

9 Y. Tian, S. Wang, E. Velasco, Y. Yang, L. Cao, L. Zhang, X. Li, Y. Lin, Q. Zhang and L. Chen, *Iscience*, 2020, **23**, 100756.

10 Y. Li, Y. Wang, J. Lu, B. Yang, X. San and Z.-S. Wu, *Nano Energy*, 2020, **78**, 105185.

11 Z. L. Zhao, Q. Wang, X. Huang, Q. Feng, S. Gu, Z. Zhang, H. Xu, L. Zeng, M. Gu and H. Li, *Energy Environ. Sci.*, 2020, **13**, 5143–5151.

20972 | *J. Mater. Chem. A*, 2022, **10**, 20964–20974

This journal is © The Royal Society of Chemistry 2022

12 J. Su, R. Ge, K. Jiang, Y. Dong, F. Hao, Z. Tian, G. Chen and L. Chen, *Adv. Mater.*, 2018, **30**, 1801351.

13 X. Cui, P. Ren, C. Ma, J. Zhao, R. Chen, S. Chen, N. P. Rajan, H. Li, L. Yu and Z. Tian, *Adv. Mater.*, 2020, **32**, 1908126.

14 L. Cao, Q. Luo, J. Chen, L. Wang, Y. Lin, H. Wang, X. Liu, X. Shen, W. Zhang and W. Liu, *Nat. Commun.*, 2019, **10**, 4849.

15 M. Retuerto, L. Pascual, F. Calle-Vallejo, P. Ferrer, D. Gianolio, A. G. Pereira, Á. García, J. Torrero, M. T. Fernández-Díaz and P. Bencok, *Nat. Commun.*, 2019, **10**, 2041.

16 M. A. Hubert, A. M. Patel, A. Gallo, Y. Liu, E. Valle, M. Ben-Naim, J. Sanchez, D. Sokaras, R. Sinclair and J. K. Nørskov, *ACS Catal.*, 2020, **10**, 12182–12196.

17 K. A. Stoerzinger, O. Diaz-Morales, M. Kolb, R. R. Rao, R. Frydendal, L. Qiao, X. R. Wang, N. B. Halck, J. Rossmeisl and H. A. Hansen, *ACS Energy Lett.*, 2017, **2**, 876–881.

18 D. Chen, T. Liu, P. Wang, J. Zhao, C. Zhang, R. Cheng, W. Li, P. Ji, Z. Pu and S. Mu, *ACS Energy Lett.*, 2020, **5**, 2909–2915.

19 X. Miao, L. Zhang, L. Wu, Z. Hu, L. Shi and S. Zhou, *Nat. Commun.*, 2019, **10**, 3809.

20 K. L. Zhou, Z. Wang, C. B. Han, X. Ke, C. Wang, Y. Jin, Q. Zhang, J. Liu, H. Wang and H. Yan, *Nat. Commun.*, 2021, **12**, 3783.

21 A. H. Motagamwala, R. Almallahi, J. Wortman, V. O. Igenegbai and S. Linic, *Science*, 2021, **373**, 217–222.

22 K.-Q. Jing, Y.-Q. Fu, Z.-N. Chen, T. Zhang, J. Sun, Z.-N. Xu and G.-C. Guo, *ACS Appl. Mater. Interfaces*, 2021, **13**, 24856–24864.

23 J. Li, J. Hu, M. Zhang, W. Gou, S. Zhang, Z. Chen, Y. Qu and Y. Ma, *Nat. Commun.*, 2021, **12**, 3502.

24 J. Huang, H. Sheng, R. D. Ross, J. Han, X. Wang, B. Song and S. Jin, *Nat. Commun.*, 2021, **12**, 3036.

25 J. Cheng, J. Yang, S. Kitano, G. Juhasz, M. Higashi, M. Sadakiyo, K. Kato, S. Yoshioka, T. Sugiyama and M. Yamauchi, *ACS Catal.*, 2019, **9**, 6974–6986.

26 Z. Wang, W. Gao, Q. Xu, X. Ren, S. Xu, S. Zhu, X. Niu, X. Li, R. Zhao and Y. Han, *ChemElectroChem*, 2021, **8**, 418–424.

27 Z. Yu, J. Xu, Y. Li, B. Wei, N. Zhang, Y. Li, O. Bondarchuk, H. Miao, A. Araujo, Z. Wang, J. L. Faria, Y. Liu and L. Liu, *J. Mater. Chem. A*, 2020, **8**, 24743–24751.

28 J. Xu, Z. Lian, B. Wei, Y. Li, O. Bondarchuk, N. Zhang, Z. Yu, A. Araujo, I. Amorim, Z. Wang, B. Li and L. Liu, *ACS Catal.*, 2020, **10**, 3571–3579.

29 J. Xu, J. Li, Z. Lian, A. Araujo, Y. Li, B. Wei, Z. Yu, O. Bondarchuk, I. Amorim, V. Tileli, B. Li and L. Liu, *ACS Catal.*, 2021, **11**, 3402–3413.

30 A. Li, H. Ooka, N. Bonnet, T. Hayashi, Y. Sun, Q. Jiang, C. Li, H. Han and R. Nakamura, *Angew. Chem.*, 2019, **131**, 5108–5112.

31 V. Giulimondi, S. K. Kaiser, M. Agrachev, F. Krumeich, A. H. Clark, S. Mitchell, G. Jeschke and J. Pérez-Ramírez, *J. Mater. Chem. A*, 2022, **10**, 5953–5961.

32 S. K. Kaiser, R. Lin, F. Krumeich, O. V. Safonova and J. Pérez-Ramírez, *Angew. Chem., Int. Ed.*, 2019, **58**, 12297–12304.

33 Y. Zhao, J. Hwang, M. T. Tang, H. Chun, X. Wang, H. Zhao, K. Chan, B. Han, P. Gao and H. Li, *J. Power Sources*, 2020, **456**, 227998.

34 B. Kang, X. Jin, S. M. Oh, S. B. Patil, M. G. Kim, S. H. Kim and S.-J. Hwang, *Appl. Catal., B*, 2018, **236**, 107–116.

35 H. Yan, Q. Shen, Y. Sun, S. Zhao, R. Lu, M. Gong, Y. Liu, X. Zhou, X. Jin and X. Feng, *ACS Catal.*, 2021, **11**, 6371–6383.

36 R. Ge, L. Li, J. Su, Y. Lin, Z. Tian and L. Chen, *Adv. Energy Mater.*, 2019, **9**, 1901313.

37 C. Xiong, T. Li, A. Dang, T. Zhao, H. Li and H. Lv, *J. Power Sources*, 2016, **306**, 602–610.

38 G. Nie, X. Lu, M. Chi, Y. Zhu, Z. Yang, N. Song and C. Wang, *Electrochim. Acta*, 2017, **231**, 36–43.

39 R. Mane, S. Patil, M. Shirai, S. Rayalu and C. Rode, *Appl. Catal., B*, 2017, **204**, 134–146.

40 L. Hao, L. Kang, H. Huang, L. Ye, K. Han, S. Yang, H. Yu, M. Batmunkh, Y. Zhang and T. Ma, *Adv. Mater.*, 2019, **31**, 1900546.

41 Y. Huang, Y. Li, Z. Hu, G. Wei, J. Guo and J. Liu, *J. Mater. Chem. A*, 2013, **1**, 9809–9813.

42 D. Zhang, J. Cao, X. Zhang, N. Insin, S. Wang, J. Han, Y. Zhao, J. Qin and Y. Huang, *Adv. Funct. Mater.*, 2021, **31**, 2009412.

43 Y. Ma, Y. Ma, T. Diemant, K. Cao, X. Liu, U. Kaiser, R. J. Behm, A. Varzi and S. Passerini, *Adv. Energy Mater.*, 2021, **11**, 2100962.

44 E. Moharreri, W. A. Hines, S. Biswas, D. M. Perry, J. He, D. Murray-Simmons and S. L. Suib, *Chem. Mater.*, 2018, **30**, 1164–1177.

45 D. Jing, D. Chen, G. Fan, Q. Zhang, J. Xu, S. Gou, H. Li and F. Nie, *Cryst. Growth Des.*, 2016, **16**, 6849–6857.

46 G. Li, H. Jang, S. Liu, Z. Li, M. G. Kim, Q. Qin, X. Liu and J. Cho, *Nat. Commun.*, 2022, **13**, 1270.

47 S. Hao, H. Sheng, M. Liu, J. Huang, G. Zheng, F. Zhang, X. Liu, Z. Su, J. Hu and Y. Qian, *Nat. Nanotechnol.*, 2021, **16**, 1371–1377.

48 J. Yoon, W. Choi, T. Kim, H. Kim, Y. S. Choi, J. M. Kim and W.-S. Yoon, *J. Energy Chem.*, 2021, **53**, 276–284.

49 J. Qin, H. Liu, P. Zou, R. Zhang, C. Wang and H. L. Xin, *J. Am. Chem. Soc.*, 2022, **144**, 2197–2207.

50 Y. Ren, Y. Tang, L. Zhang, X. Liu, L. Li, S. Miao, D. Sheng Su, A. Wang, J. Li and T. Zhang, *Nat. Commun.*, 2019, **10**, 4500.

51 W. Yang, Y. Zhu, F. You, L. Yan, Y. Ma, C. Lu, P. Gao, Q. Hao and W. Li, *Appl. Catal., B*, 2018, **233**, 184–193.

52 F. Li, Y.-L. Liu, G.-G. Wang, D. Yan, G.-Z. Li, H.-X. Zhao, H.-Y. Zhang and H.-Y. Yang, *J. Mater. Chem. A*, 2021, **9**, 9675–9684.

53 T. Gao, M. Glerup, F. Krumeich, R. Nesper, H. Fjellvåg and P. Norby, *J. Phys. Chem. C*, 2008, **112**, 13134–13140.

54 L. Yan, C. Zhu, J. Hao, X. Liang, Y. Bai, Q. Hu, B. Tan, B. Liu, X. Zou and B. Xiang, *Adv. Funct. Mater.*, 2021, **31**, 2102693.

55 X. Zhang, C. Chen, X. Chen, L. Wang, T. Huang and A. Yu, *ChemistrySelect*, 2019, **4**, 7455–7462.

56 P. K. Gupta, A. Bhandari, S. Saha, J. Bhattacharya and R. G. S. Pala, *J. Phys. Chem. C*, 2019, **123**, 22345–22357.

57 S. Liang, F. Teng, G. Bulgan, R. Zong and Y. Zhu, *J. Phys. Chem. C*, 2008, **112**, 5307–5315.

This journal is © The Royal Society of Chemistry 2022

J. Mater. Chem. A, 2022, **10**, 20964–20974 | **20973**

58 X. Shao, J. Ma, G. Wen and J. Yang, *Chin. Sci. Bull.*, 2010, **55**, 802–808.

59 S. B. Scott, J. E. Sørensen, R. R. Rao, C. Moon, J. Kibsgaard, Y. Shao-Horn and I. Chorkendorff, *Energy Environ. Sci.*, 2022, **15**, 1988–2001.

60 Y. Zhang, X. Zhu, G. Zhang, P. Shi and A.-L. Wang, *J. Mater. Chem. A*, 2021, **9**, 5890–5914.

61 L. K. McLeod, G. H. Spikes, R. J. Kashtiban, M. Walker, A. V. Chadwick, J. D. Sharman and R. I. Walton, *Dalton Trans.*, 2020, **49**, 2661–2670.

62 L. C. Seitz, C. F. Dickens, K. Nishio, Y. Hikita, J. Montoya, A. Doyle, C. Kirk, A. Vojvodic, H. Y. Hwang and J. K. Norskov, *Science*, 2016, **353**, 1011–1014.

20974 | *J. Mater. Chem. A*, 2022, **10**, 20964–20974

This journal is © The Royal Society of Chemistry 2022